A Physical Model of Non-stationary Blur in Ultrasound Imaging

Adrien Besson, *Student Member, IEEE,* Lucien Roquette, Dimitris Perdios, *Student Member, IEEE,* Matthieu Simeoni, *Student Member, IEEE,* Marcel Arditi, *Senior Member, IEEE,* Paul Hurley, Yves Wiaux, and Jean-Philippe Thiran, *Senior Member, IEEE,*

***Abstract*—Conventional ultrasound (US) imaging relies on delay-and-sum (DAS) beamforming which retrieves a radio-frequency (RF) image, a blurred estimate of the tissue reflectivity function (TRF). Despite the non-stationarity of the blur induced by propagation effects, most state-of-the-art US restoration approaches exploit shift-invariant models and are inaccurate in realistic situations. Recent techniques approximate the shift-variant blur using sectional methods resulting in improved accuracy. But such methods assume shift-invariance of the blur in the lateral dimension which is not valid in many US imaging configurations. In this work, we propose a physical model of the non-stationary blur, which accounts for the diffraction effects related to the propagation. We show that its evaluation results in the sequential application of a forward and an adjoint propagation operators under some specific assumptions that we define. Taking into account this sequential structure, we exploit efficient formulations of the operators in the discrete domain and provide an evaluation strategy which exhibits linear complexity with respect to the grid size. We also show that the proposed model can be interpreted in terms of common simplification strategies used to model non-stationary blur. Through simulations and *in vivo* experimental data, we demonstrate that using the proposed model in the context of maximum-a-posteriori image restoration results in higher image quality than using state-of-the-art shift-invariant models. The supporting code is available on github: https://github.com/LTS5/us-non-stationary-deconv.**

***Index Terms*—Non-stationary Blur, Ultrasound Imaging, Restoration**

I. Introduction

ULTRASOUND (US) imaging is a widely used medical imaging modality due to its non-invasiveness, relative low-cost and real time capability. By appropriately placing a US probe, usually an array of piezoelectric transducer elements, a medical doctor is able to visualize cross-section images of regions of interest in the body resulting from local variations in density and sound velocity.

The US imaging process exploits the transducer elements for both transmitting acoustic pulses and recording the response of the medium to these pulses as echo signals. The set of these signals is related to the spatial distribution of variations in acoustic impedance, i.e. in medium density and sound velocity, denoted as the tissue reflectivity function (TRF), by a US propagation operator. Due to finite aperture of the probe and bandlimited properties of each transducer element, retrieving the TRF from the echo signals is an ill-posed problem. In standard US imaging, the delay-and-sum (DAS) operator is used as an approximate inverse of the propagation operator. Such an approximation leads to a radio-frequency (RF) image, a blurred estimate of the TRF. The point-spread-function (PSF) is introduced to relate these quantities.

Because of the wave propagation and diffraction effects in the medium, the blur is spatially varying, as can be seen in Figure 1. Convolutional models, conventionally used in the context of spatially-invariant blur, fail in this context. Assuming a linear model of the non-stationary blur, evaluating it hence requires storing large 2D matrices (around 10^{10} coefficients for 2D US images) as well as performing matrix-vector products when used in the context of an iterative recovery algorithm. This is practically unfeasible with standard numerical tools.

To address this problem, many simplification strategies have been developed in the literature. Most of them are based on the assumption that the non-stationary blur can be approximated by a relatively low number of basis filters. The evaluation of the blur is then performed as a weighted sum of convolutions with the basis filters [1] (See [2] for an exhaustive description of such methods).

In this group of techniques, sectional methods are probably the most popular ones [3], [4], [5], [6], [7]. In such approaches, the image is divided into sub-regions where the blur is considered stationary. Then, by appropriately masking the image, shift-invariant convolutions are applied in each sub-region independently forming different sub-images that are interpolated to form the blurred image. In this case, the basis filters correspond to blur kernels. Other techniques rely on global [8], [9] or local [2] low-rank approximations of the non-stationary blur where the basis filters are the corresponding eigenvectors.

A. Besson, D. Perdios, M. Arditi and J.-Ph. Thiran are with the Signal Processing Laboratory 5 (LTS5), Ecole Polytechnique Fédérale de Lausanne, CH-1015, Lausanne, Switzerland.

L. Roquette, M. Simeoni and P. Hurley are with the Cognitive Computing Department, IBM Research, 8803, Ruschlikon, Switzerland.

M. Simeoni is also with Laboratoire de Communications Audiovisuelles (LCAV), Ecole Polytechnique Fédérale de Lausanne, CH-1015, Lausanne, Switzerland.

Y. Wiaux is with the Institute of Sensors, Signals and Systems, Heriot-Watt University, EH14 4AS Edinburgh, United-Kingdom.

J.-Ph. Thiran is also with the Department of Radiology, University Hospital Center (CHUV) and University of Lausanne (UNIL), CH-1011, Lausanne, Switzerland.

This work was supported in part by the UltrasoundToGo RTD project (no. 20NA21_145911), evaluated by the Swiss NSF and funded by Nano-Tera.ch with Swiss Confederation financing. This work was also supported by the UK Engineering and Physical Sciences Research Council (EPSRC, grants EP/M019306/1). The RF Verasonics system was co-funded by the FEDER program, Saint-Etienne Metropole (SME) and Conseil General de la Loire (CG42) within the framework of the SonoCardio-Protection Project lead by Prof. Pierre Croisille.

Alternatively, several recent works propose to approximate the blur with an operator that has desirable properties, e.g. diagonalizability [10] or sparsity [11], [12] in given frames.

In the context of US imaging, most of state-of-the-art restoration methods exploit shift-invariant models of the blur. In several studies, the PSF is estimated in a preliminary step either through *in vitro* measurements or by simulation [13], [14], [15], [16]. Other approaches estimate directly the PSF on the RF image using homomorphic filtering of the cepstrum [17], [18], [19], inverse filtering based on parametric [20], [21], [22] or non-parametric models [23], [24], [25] and power spectrum equalization [26].

Only few recent studies propose to model a spatially varying blur [27], [28]. In [27], Michailovich suggests a non-stationary model to approximate the frequency-dependent attenuation but does not take into account any diffraction effect. Roquette *et al.* [28] suggest a linear model of the non-stationary blur in the context of ultrafast US imaging but do not provide a feasible evaluation strategy.

Rather than modelling the non-stationary blur, several studies achieve shift-variant restoration using sectional methods [29], [30], [7] which assume lateral stationarity of the blur. These approaches are evidently not valid in situations where the diffraction effect is pronounced, such as the one displayed in Figure 1.

In this work, we propose the following contributions:

- We extend the shift-variant blur model introduced by Roquette *et al.* [28] in the context of plane-wave (PW) and diverging-wave (DW) imaging. We derive a sequential split of the PSF operator into a US propagation operator [31], [32] and a DAS operator, in the continuous domain;
- We propose an evaluation strategy of the non-stationary blur (and its adjoint) based on efficient computations of the DAS and US propagation operators in the discrete domain [33], [34]. We show that the proposed evaluation strategy can be interpreted in the context of sectional methods with fundamental differences that we describe. We demonstrate theoretically that the evaluation of the blur using the proposed strategy scales linearly with the size of the grid similarly to the evaluation of shift-invariant blur;
- We show an example application of the non-stationary blur for US image restoration. More precisely, we use the proposed model in a maximum-a-posteriori (MAP) estimation algorithm, with a generalized Gaussian distribution (GGD) prior for the TRF [16], [35]. We test the method on an extensive number of experiments, namely a numerical phantom of point reflectors, a numerical calibration phantom and two *in vivo* carotids, for both DW and PW imaging. We demonstrate that the proposed restoration method leads to an improvement of the lateral and axial resolution, compared to methods based on state-of-the-art models of the blur, on both the point-reflector and the calibration phantoms and provides a higher contrast and visual quality on *in vivo* carotid images. All the experiments presented in the paper are reproducible and supporting code is available at https://github.com/LTS5/us-non-stationary-deconv.

The remainder of the paper is organized as follows. Section II introduces the non-stationary PSF operator and Section III describes the evaluation strategy in the discrete domain. Experimental settings are described in Section IV and results are reported and discussed in Section V. Concluding remarks are given in Section VI.

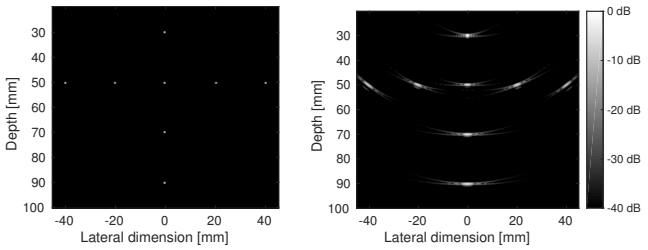

(a) (b)

Fig. 1. An example of a TRF (a) and the corresponding demodulated RF image (b) obtained with the DAS operator. We clearly see the spatially varying blur induced by classical beamforming.

II. Mathematical Modelling of Ultrasound Imaging and Continuous Level Operators

In this section, we describe a mathematical formalism of US imaging and propose formulations of the associated operators at the continuous level. Such a formalism is used to introduce a PSF operator that we sequentially split into a propagation and a DAS operators, which can benefit from fast formulations [33] detailed in Section III.

A. Notation

In the paper, we denote by $L_2(\Omega)$ the Hilbert space of the square integrable functions which take values in a space Ω. In addition, for $f, g \in L_2(\Omega)$, we denote their inner product as $\langle f, g \rangle_{L_2(\Omega)}$ and their convolution as $f * g$. The adjoint of a linear operator $\mathcal{H} : L_2(\Omega_1) \to L_2(\Omega_2)$ is given by $\mathcal{H}^\dagger : L_2(\Omega_2) \to L_2(\Omega_1)$ (See Chapter 2 of [36] for a review on linear operators).

The Hermitian transpose of a matrix $\boldsymbol{X} \in \mathbb{R}^{m \times n}$ is denoted by $\boldsymbol{X}^\dagger$ and the transpose by $\boldsymbol{X}^\top$. $\boldsymbol{X}_{\bullet J}$ is the sub-matrix formed by the restriction of $\boldsymbol{X}$ to the columns indexed by the set $J \subset \{1, \dots, n\}$. The Hadamard product between $\boldsymbol{X}$ and $\boldsymbol{Y}$ is denoted by $\boldsymbol{X} \circ \boldsymbol{Y}$.

Given a vector $\boldsymbol{a} \in \mathbb{R}^N$ and a positive real $p \in \mathbb{R}_+$, we define its p-norm as $\|\boldsymbol{a}\|_p = \sqrt[p]{\sum_{i=1}^N |a_i|^p}$.

B. Mathematical Modelling of Ultrasound Imaging

In a standard 2D pulse-echo US imaging configuration, described in Figure 2, an array of transducer elements is used to propagate an acoustic wave in a medium $\Omega \subset \mathbb{R}^2$ which contains inhomogeneities as local fluctuations in acoustic impedance, defining the TRF $\gamma \in L_2(\Omega)$ [37], [29], [33]. Depending on the desired transmit wavefront, e.g. PW, DW, focused-wave or synthetic-aperture approaches, each transducer element starts to transmit after a given delay defined by an inter-element delay profile.

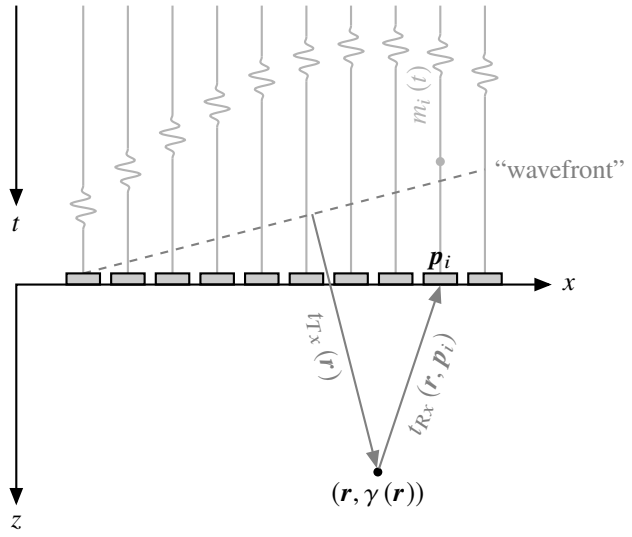

Fig. 2. Standard 2D US imaging configuration (adapted from [33]).

In a receive phase, a set of transducer elements, located at $(\boldsymbol{p}_i)_{i=1}^{N_{el}}$, $\boldsymbol{p}_i \in \mathbb{R}^2$, detect echo signals $m_i(t)$, $t \in [0,T]$, defining the following measurements

$$m(t) := \left[m_1(t), \ldots, m_{N_{el}}(t)\right] \in L_2([0,T])^{N_{el}}, \tag{1}$$

where $L_2([0,T])^{N_{el}} := L_2([0,T]) \times \cdots \times L_2([0,T])$.

The measurements $m(t)$ are related to the TRF γ by the propagation of the US wave during the time interval $[0,T]$. It can be demonstrated using the Born approximation that a linear operator $\mathcal{H} : \gamma \mapsto m$, called the propagation operator, relates the TRF to the measurements [31], [33], [34].

A standard US image reconstruction process reconstructs the RF image $\hat{\gamma}$, an estimate of the TRF γ, which should be ideally close to γ. This process involves a second operator $\mathcal{D} : m \mapsto \hat{\gamma}$ known as the DAS operator and described in Section II-D.

Using the operators introduced above, we define the US imaging procedure as a mapping between the TRF and the RF image

$$\begin{aligned} \mathcal{K} : L_2(\Omega) &\to L_2(\Omega) \\ \gamma &\mapsto \hat{\gamma} = \mathcal{D}\mathcal{H}\{\gamma\}. \end{aligned} \tag{2}$$

The operator $\mathcal{K}$ is denoted as the PSF operator since it characterizes the blur introduced by the imaging process when approximating γ by $\hat{\gamma}$. A further description of the PSF is given in Section II-E.

C. Ultrasound Propagation Operator

The proposed physical modelling of wave propagation is based on the pulse-echo spatio-temporal impulse response model introduced by Stepanishen [38]. Furthermore, the effect of the transducer element surface is approximated by a directivity function using a far-field assumption [39]. Under this approximation, we can express the element-raw data received on the i-th channel as

$$m_i(t) = \int_{\boldsymbol{r}\in\Omega} o(\boldsymbol{p}_i, \boldsymbol{r})\, v_{pe}(t - \tau(\boldsymbol{r}, \boldsymbol{p}_i))\, \gamma(\boldsymbol{r})\, d\boldsymbol{r}, \tag{3}$$

where $o(\boldsymbol{p}_i, \boldsymbol{r})$ accounts for the spatial directivity and decay of the reflected wave and $v_{pe}(t)$ is the pulse-echo waveform [40] which depends on the transducer impulse response and the excitation signal. The round trip time-of-flight $\tau(\boldsymbol{r}, \boldsymbol{p}_i)$ is defined as

$$\tau(\boldsymbol{r}, \boldsymbol{p}_i) = t_{Tx}(\boldsymbol{r}) + t_{Rx}(\boldsymbol{r}, \boldsymbol{p}_i), \tag{4}$$

where $t_{Rx}(\boldsymbol{r}, \boldsymbol{p}_i) = \|\boldsymbol{r} - \boldsymbol{p}_i\|_2 / c$ denotes the propagation delay in receive and $t_{Tx}(\boldsymbol{r})$ is the propagation delay in transmit, supposed to be independent from the location of the emitters assuming a planar wavefront in PW imaging [41] or a spherical wavefront in DW imaging [42].

Equation (3) can be compactly expressed in terms of a linear integral operator acting on the TRF $\gamma \in L_2(\Omega)$ and outputting the measurements

$$m(t) = \mathcal{H}\{\gamma\}(t), \tag{5}$$

where $\mathcal{H} : L_2(\Omega) \to L_2([0,T])^{N_{el}}$ is an operator whose i-th component is given by

$$(\mathcal{H}\{\gamma\})_i(t) = \int_{\boldsymbol{r}\in\Omega} o(\boldsymbol{p}_i, \boldsymbol{r})\, v_{pe}(t - \tau(\boldsymbol{r}, \boldsymbol{p}_i))\, \gamma(\boldsymbol{r})\, d\boldsymbol{r}. \tag{6}$$

D. Delay-and-sum Operator

Starting from the measurements $m(t)$, standard US image reconstruction exploits the well-known delay-and-sum (DAS) algorithm for computing the following RF image:

$$\hat{\gamma}(\boldsymbol{r}) = \sum_{i=1}^{N_{el}} a(\boldsymbol{p}_i, \boldsymbol{r})\, m_i(\tau(\boldsymbol{r}, \boldsymbol{p}_i)) \tag{7}$$

where $a(\boldsymbol{p}_i, \boldsymbol{r})$ accounts for the aperture-apodization weights, commonly applied to reduce the sidelobe levels. The intuition behind DAS is rather simple. In order to estimate the TRF at location $\boldsymbol{r}$, we sum echo signals originating from this point and reaching the transducer elements at each given time-of-flight. Reformulating DAS in terms of a linear integral operator acting on $m(t) \in L_2([0,T])^{N_{el}}$ is also straightforward,

$$\begin{aligned} \hat{\gamma}(\boldsymbol{r}) &= \int_0^T \sum_{i=1}^{N_{el}} a(\boldsymbol{p}_i, \boldsymbol{r})\, \delta(t - \tau(\boldsymbol{r}, \boldsymbol{p}_i)) m_i(t)\, dt \\ &= \mathcal{D}\{m\}(\boldsymbol{r}), \end{aligned} \tag{8}$$

where $\mathcal{D} : L_2([0,T])^{N_{el}} \to L_2(\Omega)$.

E. From the Point-spread-sunction Operator to the Point-spread-function

We are now equipped with the two operators $\mathcal{D}$ and $\mathcal{H}$ that can be injected in (2) to compute the PSF operator as follows [28]:

$$\begin{aligned} \hat{\gamma}(\boldsymbol{r}) &\overset{(7)}{=} \sum_{i=1}^{N_{el}} a(\boldsymbol{p}_i, \boldsymbol{r})\, m_i(\tau(\boldsymbol{r}, \boldsymbol{p}_i)) \\ &\overset{(3)}{=} \int_{\boldsymbol{s}\in\Omega} \sum_{i=1}^{N_{el}} a(\boldsymbol{p}_i, \boldsymbol{r})\, o(\boldsymbol{p}_i, \boldsymbol{s})\, v_{pe}(\tau(\boldsymbol{r}, \boldsymbol{p}_i) - \tau(\boldsymbol{s}, \boldsymbol{p}_i))\, \gamma(\boldsymbol{s})\, d\boldsymbol{s} \\ &= \mathcal{K}\{\gamma\}(\boldsymbol{r}), \end{aligned} \tag{9}$$

where $\mathcal{K}$ is defined as,

$$\begin{aligned}\mathcal{K} &: L_2(\Omega) \to L_2(\Omega)\\ \gamma &\mapsto \int_{\boldsymbol{s}\in\Omega} \gamma(\boldsymbol{s})\, k(\cdot,\boldsymbol{s})\, d\boldsymbol{s},\end{aligned} \tag{10}$$

where $k : \Omega \times \Omega \to \Omega$, the bivariate kernel of $\mathcal{K}$, defines the PSF and can be expressed as follows

$$k(\boldsymbol{r},\boldsymbol{s}) = \sum_{i=1}^{N_{el}} a(\boldsymbol{p}_i,\boldsymbol{r})\, o(\boldsymbol{p}_i,\boldsymbol{s})\, v_{pe}(\tau(\boldsymbol{r},\boldsymbol{p}_i) - \tau(\boldsymbol{s},\boldsymbol{p}_i)). \tag{11}$$

Equipped with the above defined PSF operator, the restoration problem can be stated as:

$$\text{Recover } \gamma \text{ from } \hat{\gamma} = \mathcal{K}\{\gamma\}. \tag{12}$$

F. Adjoint of the Point-spread-function Operator

In most restoration methods, the adjoint operator $\mathcal{K}^\dagger$ is required to solve Problem (12). For instance, restoration approaches that require to solve a convex optimization problem need to compute the gradient of a data fidelity term, usually expressed using the squared ℓ_2-norm. Such a gradient is defined as $\mathcal{K}^\dagger(\mathcal{K}\gamma - m)$. At the continuous operator level, the adjoint PSF operator can also be decomposed in terms of the adjoint DAS and adjoint propagation operator,

$$\mathcal{K}^\dagger = \mathcal{H}^\dagger \mathcal{D}^\dagger,\ \mathcal{K}^\dagger : L_2(\Omega) \to L_2(\Omega), \tag{13}$$

with,

$$\mathcal{H}^\dagger : L_2([0,T])^{N_{el}} \to L_2(\Omega),\ \mathcal{D}^\dagger : L_2(\Omega) \to L_2([0,T])^{N_{el}}.$$

In addition, the adjoint operators $\mathcal{D}^\dagger$ and $\mathcal{H}^\dagger$ are directly obtained from their definitions,

$$\langle \gamma, \mathcal{H}^\dagger m\rangle_{L_2(\Omega)} = \langle \mathcal{H}\gamma, m\rangle_{L_2([0,T])^{N_{el}}}, \tag{14}$$

$$\langle \gamma, \mathcal{D} m\rangle_{L_2(\Omega)} = \langle \mathcal{D}^\dagger \gamma, m\rangle_{L_2([0,T])^{N_{el}}}, \tag{15}$$

by simply flipping the order of integration over Ω and $[0,T]$ [33]. These changes are legitimate thanks to the square integrability of the involved functions.

Consequently, the adjoint operator of the propagation model is given by

$$\mathcal{H}^\dagger\{m\}(\boldsymbol{r}) = \sum_{i=1}^{N_{el}} \int_0^T o(\boldsymbol{p}_i,\boldsymbol{r})\, m_i(t)\, v_{pe}(t - \tau(\boldsymbol{r},\boldsymbol{p}_i))\, dt, \tag{16}$$

and the adjoint DAS operator by

$$\left(\mathcal{D}^\dagger\{\gamma\}\right)_i(t) = \int_{\boldsymbol{r}\in\Omega} a(\boldsymbol{p}_i,\boldsymbol{r})\delta(t - \tau(\boldsymbol{r},\boldsymbol{p}_i))\gamma(\boldsymbol{r})d\boldsymbol{r},\ i = 1,\dots,N_{el}. \tag{17}$$

Interestingly, the adjoint PSF operator can be expressed immediately using the PSF kernel defined in (11), by flipping the two arguments, i.e. using a symmetrised kernel $\tilde{k}(\boldsymbol{r},\boldsymbol{s}) = k(\boldsymbol{s},\boldsymbol{r})$.

III. Evaluation Strategy of the Non-stationary Blur in the Discrete Domain and Resulting Complexity

In this section, we express the non-stationary blur over a regular grid. More precisely, the TRF $\boldsymbol{\Gamma} \in \mathbb{R}^{N_x \times N_z}$ is defined on a regular grid $\Omega_\gamma = \{(x_u, z_v) \in \Omega, u = 1,\dots,N_x, v = 1,\dots,N_z\}$ and the RF image $\hat{\boldsymbol{\Gamma}} \in \mathbb{R}^{\hat{N}_x \times \hat{N}_z}$ is defined on a second regular grid $\Omega_{\hat{\gamma}} = \left\{(x_k, z_l) \in \Omega, k = 1,\dots,\hat{N}_x, l = 1,\dots,\hat{N}_z\right\}$.

A. Common Simplification Strategies

We first proceed with several comments on the PSF kernel defined in (11):

- If we assume that $\gamma(\boldsymbol{r}) = \delta(\boldsymbol{r} - \boldsymbol{r}_0)$, with $\boldsymbol{r}_0 \in \Omega$, then
$$\hat{\gamma}(\boldsymbol{r}) = k(\boldsymbol{r},\boldsymbol{r}_0), \tag{18}$$
leading to a natural interpretation of k as the PSF, i.e. the response of the US system to a TRF composed of a single point reflector located at $\boldsymbol{r}_0$;
- In a spatially invariant case, the bivariate kernel $k(\boldsymbol{r},\boldsymbol{s})$ is simplified to a univariate one leading to $k(\boldsymbol{r},\boldsymbol{s}) = k(\boldsymbol{r} - \boldsymbol{s})$. Under this approximation, Equation (10) becomes the standard bi-dimensional analytical convolution;
- Considering that Ω is discretized with N_g grid points, the evaluation of (10) requires $O\left(N_g^2 N_{el}\right)$ operations, which is not practically computable on current 2D US imaging configurations where N_g is of the order of 10^4 to 10^6.

Thus, we are facing the typical case of a non-stationary linear blur that can be neither evaluated nor stored in realistic imaging scenarios. At this point, common simplifications strategies detailed in Section I are available:

- Shift-invariant blur: We consider a single blur kernel $k_0(\boldsymbol{r}) = k(\boldsymbol{r},\boldsymbol{s}_0),\ \boldsymbol{s}_0 \in \Omega$ and obtaining the blur matrix $\boldsymbol{K} \in \mathbb{R}^{N_g \times N_g}$ requires $O\left(N_g N_{el}\right)$ computations. Simple shift-invariant convolution applies and we are in the case of many state-of-the-art approaches except that we use the proposed blur kernel to generate the PSF;
- Sectional methods [2], [3], [4], [5], [6], [7]: We consider a bank of P kernels $k_i(\boldsymbol{r}) = k(\boldsymbol{r},\boldsymbol{s}_i),\ \boldsymbol{s}_i \in \Omega,\ i = 1,\dots,P$ and obtaining the blur matrices $\boldsymbol{K}_i \in \mathbb{R}^{N_g \times N_g},\ i = 1,\dots,P$, requires $O\left(P N_g N_{el}\right)$ computations. Weighted convolutions apply and we are in the case of several state-of-the-art approaches [7], [29] except that we use the proposed blur kernel to generate the PSF in each subregion.
- Low-rank approximation [2], [8], [9]: They may be difficult to use due to the impossibility to compute the singular value decomposition of the matrix of non-stationary blur.

In US imaging, the blur is continuously varying in both lateral and axial dimensions and it varies differently depending on the transmission schemes. Thus, while sectional methods may be used in specific configurations, e.g. focused wave imaging where the blur can be considered invariant in the lateral dimension [7], [29], they would require an extensive amount of

blur kernels in order to provide accurate results in the general case.

In addition, the blur kernels $k_i(\boldsymbol{r})$ are not very sparse resulting in high memory footprint of the corresponding matrices. Thus, above mentioned common simplification strategies are not well suited to US imaging and alternatives may be studied.

B. Proposed Evalutation Strategy

We tackle the problem in a completely different manner. We propose to derive a computationally efficient way to evaluate the physically-based non-stationary kernel with no further simplifying assumption.

In Section II, we have established a decomposition of the PSF operator, $\mathcal{K} : L_2(\Omega) \rightarrow L_2(\Omega)$ and its adjoint, in terms of the propagation operator $\mathcal{H}$ and DAS operator $\mathcal{D}$. This is a key property when deriving a computationally efficient formulation of the PSF operator relating the TRF to the RF image, each expressed over a specific grid,

$$\boldsymbol{K} : \mathbb{R}^{N_x \times N_z} \rightarrow \mathbb{R}^{\hat{N}_x \times \hat{N}_z},\ \hat{\boldsymbol{\Gamma}} = \boldsymbol{K}\boldsymbol{\Gamma}. \tag{19}$$

In particular, we have the discrete equivalent of the decomposition,

$$\mathcal{K} = \mathcal{D}\mathcal{H} \longrightarrow \boldsymbol{K} = \boldsymbol{D}\boldsymbol{H}, \tag{20}$$

where,

$$\boldsymbol{D} : \mathbb{R}^{N_t \times N_{el}} \rightarrow \mathbb{R}^{\hat{N}_x \times \hat{N}_z},\ \boldsymbol{H} : \mathbb{R}^{N_x \times N_z} \rightarrow \mathbb{R}^{N_t \times N_{el}}. \tag{21}$$

The above defined operators allow us to define the discrete counterpart of the continuous deconvolution problem as:

$$\text{Recover } \boldsymbol{\Gamma} \text{ from } \hat{\boldsymbol{\Gamma}} = \boldsymbol{K}\boldsymbol{\Gamma}. \tag{22}$$

The remaining of this section defines fast formulations of the discrete operators $\boldsymbol{D}$ and $\boldsymbol{H}$ from their continuous counterpart. For the sake of simplicity, the grids supporting both the RF and TRF images are assumed to be the same. The pseudo raw data generated when computing $\boldsymbol{M} = \boldsymbol{H}\boldsymbol{\Gamma} \in \mathbb{R}^{N_t \times N_{el}}$ are expressed with a uniform time spacing

$$\boldsymbol{M}_{ki} = m_i(t_k),\ i = 1, \ldots, N_{el},\ k = 1, \ldots, N_t, \tag{23}$$

associated to a given sampling frequency f_s.

C. Fast Propagation Operator and its Adjoint

Based on our previous work [33], the i-th component of the integral operator defined in (6) can be reformulated as the following convolution,

$$\left(\mathcal{H}\{\gamma\}\right)_i(t) = v_{pe} *_t \mathcal{G}_i\{\gamma\}(t), \tag{24}$$

where $*_t$ denotes the analytical convolution over the time dimension and $\mathcal{G}_i : L_2(\Omega) \rightarrow L_2([0,T])$ is defined by

$$\mathcal{G}_i\{\gamma\}(t) = \int_{\boldsymbol{r}\in\Omega} o(\boldsymbol{p}_i, \boldsymbol{r})\, \gamma(\boldsymbol{r}) \delta(t - \tau(\boldsymbol{r}, \boldsymbol{p}_i)) d\boldsymbol{r}. \tag{25}$$

Alternatively, $\mathcal{G}_i\{\gamma\}(t)$ can be expressed as

$$\mathcal{G}_i\{\gamma\}(t) = \int_{\boldsymbol{r}\in\Omega} o(\boldsymbol{p}_i, \boldsymbol{r})\, \gamma(\boldsymbol{r}) \delta(g_i(t, \boldsymbol{r}))\, d\boldsymbol{r}, \tag{26}$$

where $g_i(t, \boldsymbol{r}) = t - \tau(\boldsymbol{r}, \boldsymbol{p}_i)$.

Using the co-area formula, Equation (26) can be re-written as the following line integral [33],

$$\mathcal{G}_i\{\gamma\}(t) = \int_{\boldsymbol{r}\in S_i(t)} \frac{o(\boldsymbol{p}_i, \boldsymbol{r})\, \gamma(\boldsymbol{r})}{\mid \nabla_{\boldsymbol{r}} g_i(t, \boldsymbol{r}) \mid} d\sigma(\boldsymbol{r}), \tag{27}$$

where $S_i(t)$ is the 0-level set of the function $g_i(t, \boldsymbol{r})$ given by

$$S_i(t) = \{\boldsymbol{r} \in \Omega : g_i(t, \boldsymbol{r}) = 0\}. \tag{28}$$

By an appropriate reparameterization of $S_i(t)$ described in our previous work [33], [34], Equation (27) can be expressed as

$$\mathcal{G}_i\{\gamma\}(t) = \int_{\alpha\in\mathbb{R}} \frac{o(\boldsymbol{p}_i, \boldsymbol{r}(\alpha, \boldsymbol{p}_i, t))\, \gamma(\boldsymbol{r}(\alpha, \boldsymbol{p}_i, t))}{\mid \nabla_{\boldsymbol{r}} g_i(t, \boldsymbol{r}(\alpha, \boldsymbol{p}_i, t)) \mid} |J_{\boldsymbol{r}}| d\alpha, \tag{29}$$

where $\boldsymbol{r}(\alpha, \boldsymbol{p}_i, t) = (\alpha, z(\alpha, \boldsymbol{p}_i, t))$ and $|J_{\boldsymbol{r}}| : \mathbb{R}^2 \rightarrow \mathbb{R}$ denotes the Jacobian associated with the change of variable.

The discretization of the integral over α leads to

$$\left(\mathcal{H}\{\gamma\}\right)_i(t) \approx \left[v_{pe} *_t \left(\sum_{j=1}^{N_x} w_j(\boldsymbol{p}_i, \cdot)\, \gamma\left(\boldsymbol{r}\left(\alpha_j, \boldsymbol{p}_i, \cdot\right)\right) \right) \right](t), \tag{30}$$

where $w_j(\boldsymbol{p}_i, t)$ accounts for the spatial directivity, the decay of the reflected wave, the Jacobian, the gradient of g_i and the weights related to the numerical approximation of the integral.

Discretizing (30) with respect to t leads to

$$(\boldsymbol{H}\boldsymbol{\Gamma})_{li} \approx \left(\boldsymbol{V}_{pe}\hat{\boldsymbol{m}}_i\right)_l,\ l = 1, \ldots, N_t, \tag{31}$$

where $\boldsymbol{V}_{pe} \in \mathbb{R}^{N_t \times N_t}$ is the Toeplitz matrix associated with the discrete convolution with $\boldsymbol{v}_{pe} \in \mathbb{R}^{N_t}$ and $\hat{\boldsymbol{m}}_i \in \mathbb{R}^{N_t}$ is defined element-wise as

$$\hat{\boldsymbol{m}}_i(t_l) = \sum_{j=1}^{N_x} w_j(\boldsymbol{p}_i, t_l)\, \gamma\left(\boldsymbol{r}\left(\alpha_j, \boldsymbol{p}_i, t_l\right)\right). \tag{32}$$

It can be noticed that (31) approximates the continuous convolution in (30) by its discrete counterpart which is crucial in the acceleration of the forward operator. Without loss of generality, we consider a "half-padded" convolution [43] with zero-padding at the boundary which explains why $\boldsymbol{V}_{pe}$ is a square matrix. "Fully-padded" and "non-padded" convolutions as well as alternative boundary methods may also be considered. Since we work on a discrete grid Ω_γ, we have to introduce N_x interpolation operators $\boldsymbol{I}_j : \mathbb{R}^{N_z} \rightarrow \mathbb{R}^{N_t \times N_{el}}$ such that

$$\gamma\left(\boldsymbol{r}\left(\alpha_j, \boldsymbol{p}_i, t_l\right)\right) \approx \left(\boldsymbol{I}_j\boldsymbol{\Gamma}_{\bullet j}\right)_{li},\ j = 1, \ldots, N_x. \tag{33}$$

We can now approximate (32) as

$$\hat{\boldsymbol{m}}_i(t_l) \approx \sum_{j=1}^{N_x} w_j(\boldsymbol{p}_i, t_l) \left(\boldsymbol{I}_j\boldsymbol{\Gamma}_{\bullet j}\right)_{li}. \tag{34}$$

Consequently, the application of the discretized forward operator $\boldsymbol{H}$ over the TRF image can be formulated as

$$\boldsymbol{H}\boldsymbol{\Gamma} = \boldsymbol{V}_{pe}\left[\sum_{j=1}^{N_x} \boldsymbol{W}_j \circ \boldsymbol{I}_j\boldsymbol{\Gamma}_{\bullet j}\right] \in \mathbb{R}^{N_t \times N_{el}}, \tag{35}$$

where $\boldsymbol{W}_j \in \mathbb{R}^{N_t \times N_{el}}$ is defined element-wise as $\left(\boldsymbol{W}_j\right)_{li} = w_j\left(\boldsymbol{p}_i, t_l\right)$.

More practically, the action of the discretized forward operator defined inside the sum of (35) can be described as a sequential application of

1) a masking operation which selects the sub-region of $\boldsymbol{\Gamma}_{\bullet j}$, $j = 1, \ldots, N_x$, that interpolates the points $\left\{\gamma\left(\boldsymbol{r}\left(\alpha_j, \boldsymbol{p}_i, t_l\right)\right)\right\}_{l,i=1}^{N_t, N_{el}}$;
2) a point-wise multiplication with the weighting matrix $\boldsymbol{W}_j$;
3) a convolution with the pulse-echo waveform.

Thus, one can see the analogy with sectional methods in the context of spatially-varying blur modelling. The main difference is that the mask does not aim at isolating regions where different stationary blurs are applied. It rather selects sub-regions where the convolutions with the pulse-shape have to be applied depending on US propagation and acquisition settings (which define the parametric curves). Then, the same convolution with the pulse shape applies on every sub-regions.

The adjoint operator $\mathcal{H}^\dagger$ defined in Equation (16) can be seen as the following operation,

$$\mathcal{H}^\dagger\{m\}(\boldsymbol{r}) = \sum_{i=1}^{N_{el}} o\left(\boldsymbol{p}_i, \boldsymbol{r}\right)\left(u_{pe} *_t m_i\right)\left(\tau\left(\boldsymbol{r}, \boldsymbol{p}_i\right)\right), \tag{36}$$

where $u_{pe}(t) = v_{pe}(-t)$ is the matched filter of the pulse-echo waveform.

We introduce the convolved raw data $\tilde{m}_i = u_{pe} *_t m_i$, for $i = 1, \ldots, N_{el}$ such that

$$\mathcal{H}^\dagger\{m\}\left(\boldsymbol{r}_{sq}\right) = \sum_{i=1}^{N_{el}} o\left(\boldsymbol{p}_i, \boldsymbol{r}_{sq}\right)\tilde{m}_i\left(\tau\left(\boldsymbol{r}_{sq}, \boldsymbol{p}_i\right)\right), \tag{37}$$

for $\boldsymbol{r}_{sq} = \left(x_s, z_q\right) \in \Omega_{\hat{y}}$, $s = 1, \ldots, N_x$, $q = 1, \ldots, N_z$.

The discretization of (37) with respect to t is achieved into two steps. The first one approximates the convolved raw data $\tilde{m}_i$ with its discrete counterpart as

$$\tilde{\boldsymbol{M}}_{\bullet i} = \boldsymbol{V}_{pe}^\top \boldsymbol{M}_{\bullet i}. \tag{38}$$

To complete the discretization, we introduce N_{el} interpolation operators $\boldsymbol{I}_i' : \mathbb{R}^{N_t} \to \mathbb{R}^{N_x \times N_z}$, $i = 1, \ldots, N_{el}$, such that

$$\tilde{m}_i\left(\tau\left(\boldsymbol{r}_{sq}, \boldsymbol{p}_i\right)\right) \approx \left(\boldsymbol{I}_i' \tilde{\boldsymbol{M}}_{\bullet i}\right)_{sq},\ i = 1, \ldots, N_{el} \tag{39}$$

and (37) is approximated as

$$\left(\boldsymbol{H}^\dagger \boldsymbol{M}\right)_{sq} = \sum_{i=1}^{N_{el}} o\left(\boldsymbol{p}_i, \boldsymbol{r}_{sq}\right)\left(\boldsymbol{I}_i' \tilde{\boldsymbol{M}}_{\bullet i}\right)_{sq} \in \mathbb{R}. \tag{40}$$

The adjoint propagation operator $\boldsymbol{H}^\dagger$ expressed over the grid is therefore given by,

$$\boldsymbol{H}^\dagger \boldsymbol{M} = \sum_{i=1}^{N_{el}} \boldsymbol{O}_i \circ \boldsymbol{I}_i'\left(\boldsymbol{V}_{pe}^\top \boldsymbol{M}_{\bullet i}\right) \in \mathbb{R}^{N_x \times N_z}, \tag{41}$$

where $\boldsymbol{O}_i \in \mathbb{R}^{N_x \times N_z}$ is defined element-wise as $\left(\boldsymbol{O}_i\right)_{sq} = o\left(\boldsymbol{p}_i, \boldsymbol{r}_{sq}\right)$.

Similarly to the forward operator, the action of the discretized adjoint operator defined inside the sum of (41) can be seen as the application of:

1) a convolution of $\boldsymbol{M}_{\bullet i}$ with the matched filter of the pulse-echo waveform;
2) a masking operation which selects the sub-region of the $\boldsymbol{M}_{\bullet i}$ that interpolates the points $\left\{\tilde{m}_i\left(\tau\left(\boldsymbol{r}_{sq}, \boldsymbol{p}_i\right)\right)\right\}_{s,q=1}^{N_x, N_z}$;
3) a point-wise multiplication with $\boldsymbol{O}_i$.

The same remarks as for the discretized forward operator hold.

D. Fast Delay-and-sum Operator and its Adjoint

The DAS operator, defined in (7), can be seen as an approximation of the adjoint operator $\mathcal{H}^\dagger$ under the following assumptions:

- The pulse-echo wavelet is a Dirac delta, i.e. $v_{pe}(t) = \delta(t)$;
- The apodization weights replace the spatial directivity and the decay $1/\boldsymbol{r}$ of the reflected wave.

Thus, the application of the discretized DAS operator on the grid is directly defined by the interpolation operation introduced in (41) as

$$\boldsymbol{DM} = \sum_{i=1}^{N_{el}} \boldsymbol{A}_i \circ \boldsymbol{I}_i \boldsymbol{M}_{\bullet i} \in \mathbb{R}^{N_x \times N_z}, \tag{42}$$

where $\boldsymbol{A}_i \in \mathbb{R}^{N_x \times N_z}$ is defined element-wise as $\left(\boldsymbol{A}_i\right)_{sq} = a\left(\boldsymbol{p}_i, \boldsymbol{r}_{sq}\right)$.

the application of the discretized adjoint DAS operator $\boldsymbol{D}^\dagger$ expressed over the grid can be deduced from (35) as

$$\boldsymbol{D}^\dagger \boldsymbol{\Gamma} = \sum_{j=1}^{N_x} \boldsymbol{W}_j \circ \boldsymbol{I}_j \boldsymbol{\Gamma}_{\bullet j} \in \mathbb{R}^{N_t \times N_{el}}, \tag{43}$$

where the apodization weights are used in the computation of $\boldsymbol{W}_j$.

E. Computation Complexity of the Point-spread-function Operator

The application of the discretized PSF operator over the grid $\boldsymbol{K} : \mathbb{R}^{N_x \times N_z} \to \mathbb{R}^{N_x \times N_z}$ requires *a priori* $O((N_x N_z)^2 N_{el})$ operations using (11). Such a complexity prevents its use in realistic imaging cases, where $N_x N_z$ ranges between 10^4 and 10^6 and N_{el} is few hundreds.

To solve the above limitation, we propose to decompose the computation of $\boldsymbol{K\Gamma}$ as follows:

$$\boldsymbol{K\Gamma} = \boldsymbol{D}(\boldsymbol{H\Gamma}), \tag{44}$$

where $\boldsymbol{H\Gamma}$ is first performed, generating a pseudo raw data $\boldsymbol{M}$, followed by the application of the DAS $\boldsymbol{DM}$.

The computation of $\boldsymbol{HX}$ requires to perform the following operations:

1) N_x interpolations $\boldsymbol{I}_j \boldsymbol{\Gamma}_{\bullet j}$ where each interpolation has a computational complexity of $O(L N_t N_{el})$ with L the support of the interpolation kernel ($L << N_z$);
2) N_x point-wise multiplications with $\boldsymbol{W}_j$, each of which having a cost of $O(N_{el} N_t)$;
3) N_x convolutions with v_{pe} each of which with a complexity of $O(N_t \log N_t)$.

The overall computation complexity of $\boldsymbol{H\Gamma}$ is therefore:

$$\begin{aligned}\text{Cost}(\boldsymbol{H\Gamma}) &= O\left(L N_x N_{el} N_t + N_x N_{el} N_t + N_x N_t \log N_t\right) \\ &= O\left(N_x N_{el} N_t\right),\end{aligned} \tag{45}$$

since $\log N_t \ll N_{el}$ and $L \ll N_l$ in US imaging.

The computation of $\boldsymbol{DM}$ necessitates rather similar operations as the one described above, apart from the convolution:

1) N_{el} interpolations $\boldsymbol{I}_i\boldsymbol{M}_{\bullet i}$ where each interpolation has a computational complexity of $O(L'N_xN_z)$ with L' the support of the interpolation kernel ($L' \ll N_t$);
2) N_{el} point-wise multiplications with $\boldsymbol{A}_i$, each of which having a cost of $O(N_xN_z)$.

The computational complexity of $\boldsymbol{DM}$ is:

$$\text{Cost}(\boldsymbol{DM}) = O(L'N_{el}N_xN_z + N_{el}N_xN_z) \quad (46)$$
$$= O(N_{el}N_xN_z). \quad (47)$$

The overall complexity of the operation $\boldsymbol{K\Gamma}$ can be easily deduced from (46) and (47) as:

$$\text{Cost}(\boldsymbol{K\Gamma}) = O(N_{el}N_x(N_t + N_z)) \quad (48)$$
$$\approx O(N_{el}N_xN_z), \quad (49)$$

since $N_t \approx N_z$ in standard US imaging configurations. Thus we have the following:

$$\text{Cost}(\boldsymbol{KX}) \ll O((N_xN_z)^2N_{el}). \quad (50)$$

An equivalent reasoning for the computation of the adjoint operation $\boldsymbol{K}^\dagger\hat{\boldsymbol{\Gamma}}$ leads to the same computational complexity as the forward operation. Indeed, the only difference between the two computations resides in the convolution which is negligible in the computational cost.

Thus, the proposed sequential split assumption results in a significant decrease of the computational complexity from quadratic to linear with respect to N_xN_z.

Compared to the common strategies described in Section III-A we can draw the following conclusions. If we assume that shift-variant blurs have been stored as matrices of size $N_x^b \times N_z^b$, where $N_z^b < N_z$ and $N_x^b < N_x$ (as it is often the case), their evaluations would require $O(N_xN_z \log N_xN_z)$ computations using a Fourier-domain approach or $O\left(N_x^bN_z^bN_xN_z\right)$ otherwise.

Using the Fourier-domain approach, the complexity is usually slightly lower than the proposed approach since $\log N_xN_z < N_{el}$ but the method does not scale as well as the proposed approach with respect to the grid size. Otherwise, the complexity highly depends on the size of the blur matrix while the complexity remains linear with respect to the grid size.

IV. Experiments

This section describes the imaging configurations, for both DW and PW, used to evaluate the proposed non-stationary PSF estimation against state-of-the-art methods. It also describes the ℓ_p-based convex optimization method used to solve (22).

A. Diverging Wave Imaging Configuration

A simulated experiment is performed with a standard phased-array probe (P4-2v) whose characteristics are given in Table I. A single diverging wave (2.5 MHz, 1-cycle sinusoidal wave) is transmitted with a corresponding virtual point source located at z_n equal to -2.9 mm and laterally centered. No apodization is used on transmit.

TABLE I
Probe Characteristics

	Diverging wave P4-2v	Plane wave L11-4v	Plane wave L12-5 50mm
Element number	64	128	128
Center frequency	2.7 MHz	5.133 MHz	7.8 MHz
Sampling frequency	10.8 MHz	20.832 MHz	31.2 MHz
Element width	255 µm	270 µm	Unknown
Pitch	280 µm	300 µm	195 µm
Elevation focus	60 mm	20 mm	Unknown

The data are acquired on a numerical point-reflector phantom with eight reflectors with unit amplitude and located at positions described on Figure 3(a). The simulation software used in this experiment is Field II [40].

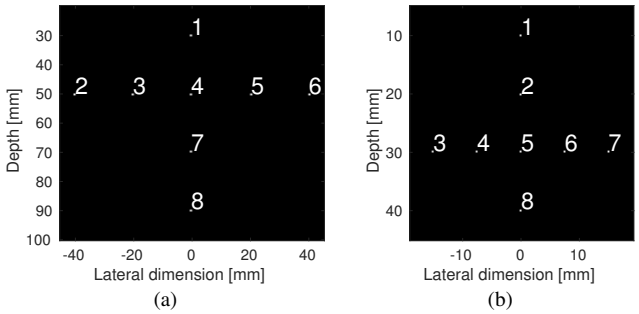

(a) (b)

Fig. 3. Numerical point-reflector phantoms used for (a) diverging wave and (b) plane wave imaging configurations.

B. Plane Wave Imaging Configurations

Two standard linear-array probes are used, namely the L11-4v and the L12-5 50mm, whose characteristics are given in Table I.

The L11-4v is used in two simulated configurations (using Field II) for which a single plane wave (5.208 MHz, 2.5-cycle-excitation) with normal incidence is transmitted without apodization:

- A point-reflector phantom with reflectors described in Figure 3(b);
- the PICMUS numerical phantom[1], whose example B-mode image is displayed on Figure 4.

The L12-5 50mm is used to acquire *in vivo* measurements of two carotids on a Verasonics US scanner (Redmond, WA, USA). A single plane wave (5 MHz, 1-cycle excitation) with normal incidence is transmitted without apodization.

C. Proposed ℓ_p-based Restoration Method

We use a ℓ_p-norm minimization, one of the most recent methods introduced in US image restoration [16], [44], [35], [45], [24], [28]. Since the discretized PSF operator has been described as a tensor in Section III-C, we have to introduce the reshaping operator $\boldsymbol{P} : \mathbb{R}^{N_x \times N_z} \to \mathbb{R}^{N_xN_z}$, such that $\boldsymbol{\gamma} = \boldsymbol{P\Gamma} \in$

[1] https://www.creatis.insa-lyon.fr/EvaluationPlatform/picmus/index.html

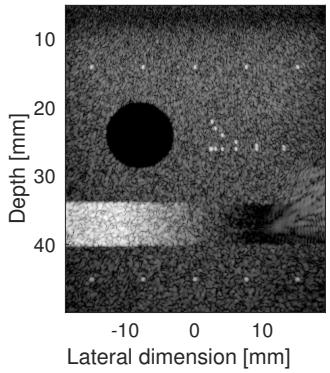

Fig. 4. Log-compressed B-mode image of the PICMUS numerical phantom.

$\mathbb{R}^{N_x N_z}$. We are therefore interested in solving the following optimization problem,

$$\min_{\tilde{\boldsymbol{\gamma}} \in \mathbb{R}^{N_x N_z}} \lambda \|\tilde{\boldsymbol{\gamma}}\|_p^p + \frac{1}{2} \left\|\hat{\boldsymbol{\gamma}} - \tilde{\boldsymbol{K}}\tilde{\boldsymbol{\gamma}}\right\|_2^2, \tag{51}$$

where $\tilde{\boldsymbol{K}} = \boldsymbol{P}\boldsymbol{K}\boldsymbol{P}^\dagger \in \mathbb{R}^{N_x N_z \times N_x N_z}$ accounts for the discretized PSF operator and $\hat{\boldsymbol{\gamma}} = \boldsymbol{P}\hat{\boldsymbol{I}} \in \mathbb{R}^{N_x N_z}$, where $\hat{\boldsymbol{I}}$ is the RF image acquired by the US imaging system. In the objective function minimized in (51), the first term is the prior, the second term is the data-fidelity, $\lambda \in \mathbb{R}_+$ is a regularization parameter and p is a real so that $1 \leq p \leq 2$ [46].

The values of p are set to 1, 4/3 or 3/2, depending on the experiment, similar to the values used in [16] since their corresponding proximity operator are analytically defined (Appendix A). The optimization algorithm used to solve the restoration problem is the fast iterative shrinkage thresholding algorithm (FISTA) described in Appendix A [47].

Three different PSF estimation techniques are compared:

- The proposed non-stationary PSF;
- a stationary PSF estimated from the data using the method described in [29], denoted as stationary PSF 1;
- a stationary PSF previously simulated on Field II using a phantom made of a single scatterer located at 25 mm for PW imaging and 45 mm for DW imaging, denoted as stationary PSF 2.

The restoration is performed on RF images, obtained by applying the DAS operator on the element-raw data. The image grid spacing is set to one third of the wavelength in the lateral direction and one eighth of the wavelength in the axial direction. The apodization used in receive is the element-directivity according to Selfridge *et al.* [39].

D. Implementation Details

The methods are implemented using MATLAB[2].

For the stationary methods, we store the PSF in a matrix form and we compute the shift-invariant convolutions using the Fourier domain approach.

For the proposed non-stationary blur, we implement parallelized matrix-free evaluation of the different operators as described in [33].

[2]https://github.com/AdriBesson/epfl-ibm-code

Concerning FISTA, we consider a maximum number of 100 iterations and we set a stopping criterion if the relative evolution of the solution between two consecutive iterations is lower than 10^{-3}. The regularization parameter λ is empirically tuned for each method and each experiment. Automatic optimization of such a parameter is left for future work.

V. Results and Discussion

A. Point-reflector Experiment

For these experiments, the ℓ_p-based restoration is tested with a value of p equal to 1 since we are dealing with sparse images. The comparison is based on the axial and lateral resolution, calculated as the full-width-at-half maximum (FWHM) [48] computed on the log-compressed B-mode image. The regularization parameter is empirically set to its highest value so that all the point reflectors are visible, if possible.

Table II reports the lateral and axial resolution values for the DW configuration described in Figure 3(a). We can see that the proposed method outperforms the models based on a stationary PSF on the lateral resolution especially. This makes sense since the diffraction effect is important in DW imaging configurations resulting in significant variability in the lateral dimension. Regarding the axial resolution, it is relatively stationary along the imaging plane and the proposed method does not significantly outperform the stationary models. Figure 5 shows the B-mode images of the point-reflectors for standard DAS beamforming (top row), restoration with the proposed method (middle row) and restoration with the stationary PSF 1 (bottom row). It illustrates the benefit of the proposed method compared to stationary models for image restoration in case of imaging configurations with high lateral variability.

TABLE II
Comparison of the Methods on the Point-reflector Phantom in the Diverging Wave Experiment

	Method	1	2	3	4	5	6	7	8
Lat. Res [mm]	Prop. PSF	**0.32**	**0.19**	0.21	**0.50**	0.21	**0.21**	**0.60**	**0.60**
	Stat. PSF 1	0.90	0.21	**0.19**	1.4	**0.19**	**0.21**	2.2	2.7
	Stat. PSF 2	6.9	9.5	9.5	2.9	9.5	9.5	1.6	3.2
Ax. Res [mm]	Prop. PSF	0.43	0.21	0.42	0.24	**0.07**	**0.07**	0.21	0.21
	Stat. PSF 1	**0.28**	**0.07**	**0.08**	**0.08**	0.41	0.08	**0.08**	**0.08**
	Stat. PSF 2	0.46	3.6	3.6	0.55	3.6	3.6	0.37	0.39

When using the method with the stationary PSF 2, it can be noted that the values for both the axial and the lateral resolution are not satisfactory, except for point-reflectors 4, 7 and 8. This is due to the fact that the PSF used in the restoration experiment has been simulated with a point-reflector centered at 45 mm, close to point-reflector 4, and that point-reflectors 7 and 8 are centered as well. The high values of the resolution that one may observe in Table II are due to the fact that several points are not reconstructed. Regarding the method with the stationary PSF 1, the results are better. This can be explained by the fact that the PSF estimation method returns a sort of "averaged PSF" over the entire image, resulting in a rather uniform value of the resolution. We can

nevertheless observe a non-uniformity of the resolution with respect to depth (point-reflectors 7 and 8), which emphasizes the inability of the method to capture non-stationary blur.

In the PW experiment, it can be noticed on Table III that the proposed approach is either close to or better than the best of the methods based on a stationary PSF, which means that it represents a best compromise between lateral and axial resolution. However, the results on the lateral resolution are less striking than for the DW experiment which is justified by the reduced non-stationarity of the blur compared to the DW experiment. Regarding the stationary PSF 2, while the lateral resolution is relatively constant along the image, the values of the axial resolution is varying significantly. This is due to our choice of regularization parameter. Indeed, it is set so that all the point-reflectors are visible. When the regularization parameter is too high, the first point-reflectors that vanish are point-reflectors 3 and 7 since they are the ones with the highest mismatch with the centered PSF pattern used in the restoration.

TABLE III
COMPARISON OF THE METHODS ON THE POINT-REFLECTOR PHANTOM IN THE PLANE WAVE EXPERIMENT

	Method	1	2	3	4	5	6	7	8
Lat. Res [mm]	Prop. PSF	**0.11**	**0.11**	0.11	**0.11**	**0.11**	**0.11**	**0.10**	**0.11**
	Stat. PSF 1	**0.11**	0.12	0.11	**0.11**	0.12	0.15	0.13	0.12
	Stat. PSF 2	**0.11**	0.11	**0.10**	**0.11**	**0.11**	**0.11**	0.11	**0.11**
Ax. Res [mm]	Prop. PSF	**0.04**	0.11	**0.04**	**0.04**	**0.04**	**0.04**	**0.04**	**0.04**
	Stat. PSF 1	0.21	**0.04**	**0.04**	**0.04**	**0.04**	**0.04**	**0.04**	**0.04**
	Stat. PSF 2	**0.04**	0.22	**0.04**	0.22	0.22	0.22	**0.04**	**0.04**

With a close look on Tables II and III, one may highlight some non-uniformity in the values of the resolution obtained with the proposed method. This can be explained by several approximations made in the physical model of the blur:

- no three-dimensional propagation: The proposed model neglects the effects related to the three-dimensional propagation in the Field II simulation, especially the element height and the elevation focus;
- planar/spherical wavefront assumption: We assume that a planar or spherical wavefront, for PW and DW respectively, of constant amplitude propagates in the medium;
- grid mismatch induced by the discretization of the continuous propagation operator and the continuous medium.

B. PICMUS Phantom Experiment

In this experiment, we compare the methods based on the dB-contrast-to-noise ratio (CNR) and lateral and axial resolution, computed on the PICMUS phantom displayed in Figure 4. The CNR [48] is a measure of the contrast, calculated on the normalized envelope image, i.e. on the envelope image divided by its maximum value, as follows,

$$\mathrm{CNR} = 20\log_{10}\frac{|\mu_t - \mu_b|}{\sqrt{\frac{\sigma_t^2+\sigma_b^2}{2}}}, \tag{52}$$

where (μ_t, μ_b) and (σ_t^2, σ_b^2) are the means and the variances of the target inclusion (anechoic region of Figure 4) and the background, respectively.

The results are reported in Table IV for the ℓ_p-based restoration, with $p = 1.3$ and 1.5, and with the proposed non-stationary PSF as well as the two stationary ones.

On Table IV, one can see that the proposed PSF outperforms the other methods on the lateral resolution. Indeed, the variability of the PSF in the axial dimension is mainly due to variations of the pulse-echo waveform induced either by frequency-dependent attenuation or by near-field effects (due to the finite element height). In the proposed simulation, we are at sufficiently far-field and the frequency-dependent attenuation is not taken into account. Thus, a shift-invariant model is relatively accurate.

In order to illustrate the above remarks, Figure 6 displays the x-axis and z-axis sections corresponding to the points located at $z = 14$ mm and $x = 0$ mm and 15 mm. While the effect of the proposed method is not evident on the axial dimension (bottom row), it is significant in the lateral dimension (top row).

Regarding the results of the restoration procedure, we observe that $p = 1.3$ leads to better resolution (as can be seen on Figure 6) but lower contrast than $p = 1.5$. This can be explained by a close look at the definition of the CNR. Indeed, it may be deduced from (52) that the CNR favors piecewise-continuous regions where σ_b and σ_t tend to 0. On the contrary, high-resolution images exhibit more "spiky" behaviour in speckle region than low-resolution images which usually result in lower mean and higher variance, therefore in a lower CNR. In ℓ_p-based restoration, the value of p impacts the shape of the GGD prior, resulting in variation of the resolution of the recovered TRF. The lower p, the tighter the shape of the prior, the better the resolution and the lower the CNR.

TABLE IV
COMPARISON OF THE METHODS ON THE NUMERICAL PICMUS PHANTOM

Value of p	CNR [dB]	Method	Lat. Res. [mm] 14 mm	Lat. Res. [mm] 45 mm	Ax. Res. [mm] 14 mm	Ax. Res. [mm] 45 mm
$p = 1.5$	7.00	Prop. PSF	**0.21**	**0.35**	0.24	0.28
		Stat. PSF 1	0.25	0.46	**0.23**	0.30
		Stat. PSF 2	0.30	0.41	0.27	**0.26**
$p = 1.3$	6.00	Prop. PSF	**0.17**	**0.25**	0.20	0.24
		Stat. PSF 1	0.21	0.45	**0.17**	0.22
		Stat. PSF 2	0.27	0.36	0.20	**0.18**

C. In vivo Carotid Experiments

Low resolution demodulated RF images of the two carotids, obtained by DAS beamforming without restoration, are displayed on Figs. 7(a) and 7(e). The B-mode images of the ℓ_p-based restoration technique for the first carotid, and for $p = 1.5$, are displayed on Figs. 7(b), 7(c) and 7(d). The B-mode images of the ℓ_p-based restoration technique for the second carotid, and for $p = 1.3$, are displayed on Fig. 7(f), 7(g) and 7(h).

In order to quantify the benefits of the proposed model of the blur, we rely on the tissue-to-clutter ratio (TCR) [49] and the signal-to-noise ratio (SNR) [49] metrics. The TCR is a widely used measure of the contrast defined as the ratio between the average pixel intensity in a tissue region and in

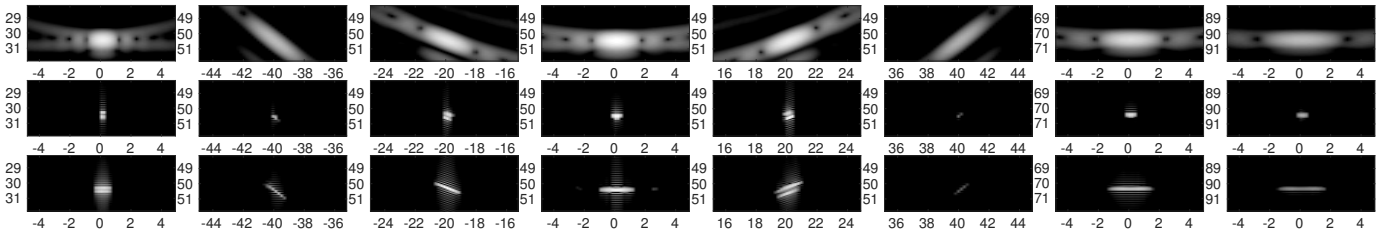

Fig. 5. Close-up of log-compressed (40 dB dynamic range) B-mode images of point-reflector 1 to point-reflector 8 (from left to right) of the DW configuration (Fig. 3(a)) obtained with standard DAS beamforming (top row), restoration with the proposed method (middle row) and restoration with the stationary PSF 1 (bottom row).

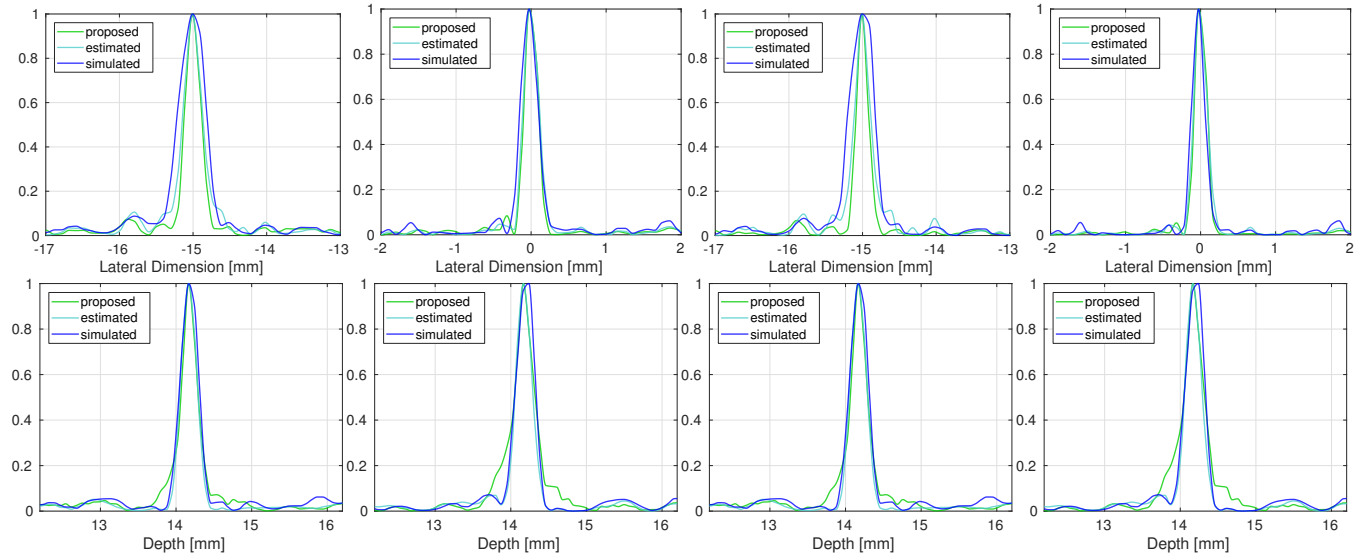

Fig. 6. x-axis (top row) and z-axis (bottom row) sections corresponding to the points located at $z = 14$ mm and $x = 0$ mm and 15 mm, for $p = 1.5$ (2 left plots) and $p = 1.3$ (2 right plots) and for the different blur models.

a background region at the same depth (to avoid bias due to time-gain compensation). Formally, it is given by

$$TCR = 20 \log_{10} \left(\frac{\mu_t}{\mu_b} \right), \tag{53}$$

where μ_t and μ_b designate mean pixel intensities inside the tissue and the background regions, respectively, calculated on the normalized envelope.

The SNR is calculated as

$$SNR = \frac{|\mu_t - \mu_b|}{\sqrt{\sigma_b^2 + \sigma_t^2}}, \tag{54}$$

where (μ_t, μ_b) and (σ_t, σ_b) are the mean and standard deviation of the pixel intensities of a tissue and a blood regions, respectively, calculated on a linearized image obtained from the log-compressed B-mode image. We choose a background region located inside the carotid artery and a tissue region located at the same depth, as described on Figure 8.

TCR and SNR values, reported on Table V, demonstrate that the proposed non-stationary model outperforms stationary models for nearly all the experiments. Regarding the impact of the value of p, the same trend as for the PICMUS experiment is observed, i.e. a lower value of p leads to a lower SNR induced by higher variance of the speckle pattern. In addition, visual assessment of the B-mode images show that the restoration methods all lead to significantly higher resolution than the unprocessed B-mode image. The deblurring effect is more pronounced for the proposed method and the stationary PSF 1 than for the stationary PSF 2, as can be seen on the artery wall. In addition, the proposed method allows a better reconstruction of the textured area, such as the speckle region under the lower artery wall, than both methods based on a stationary PSF.

TABLE V
COMPARISON OF THE METHODS ON THE IN-VIVO CAROTIDS

Value of p	Carotid number	Method	SNR [–]	TCR [dB]
$p = 1.5$	1	Prop. PSF	**49.1**	**29.5**
		Stat. PSF 1	27.9	26.2
		Stat. PSF 2	38.6	28.1
$p = 1.3$	2	Prop. PSF	21.5	**30.5**
		Stat. PSF 1	21.1	24.4
		Stat. PSF 2	**36.1**	28.4

D. On Computational Times of the Proposed Strategy

In Section III-E, we have derived the computational complexity of the proposed evaluation strategy and demonstrated that it scales linearly with respect to the grid size. In this Section, we discuss the practical implications of this in terms of computational times necessary to evaluate the forward blur operator.

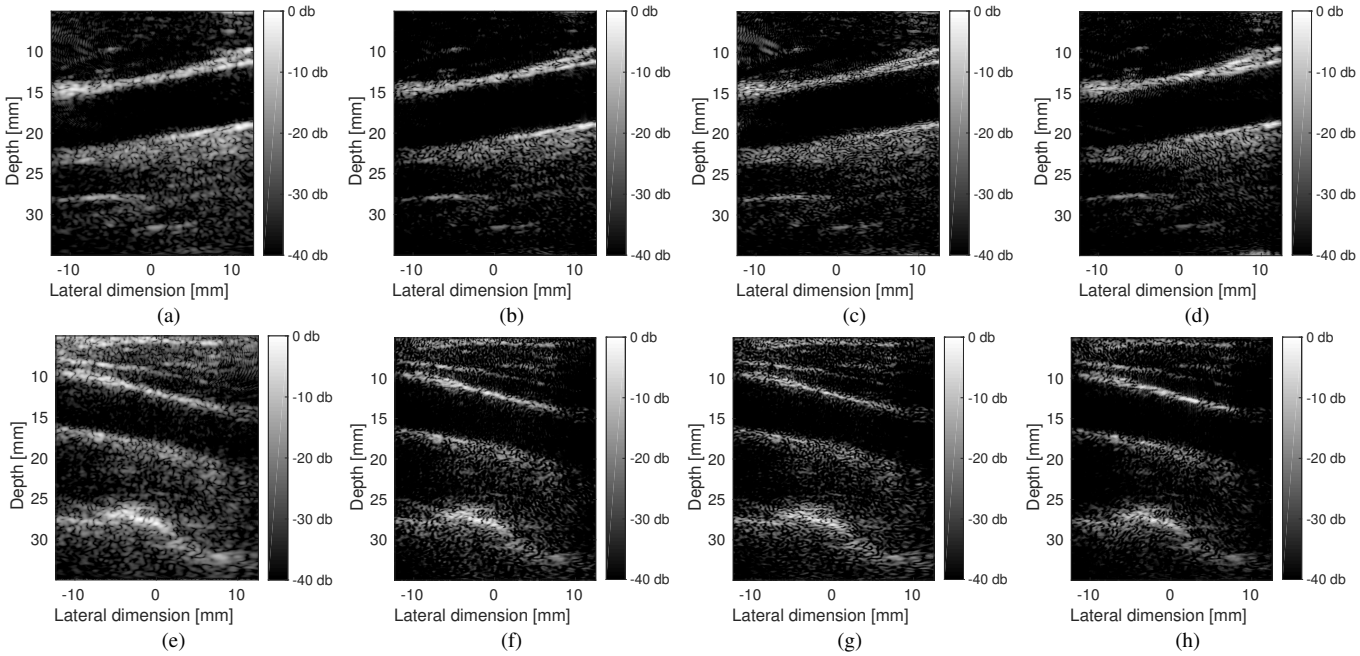

Fig. 7. (a)-Low resolution (LR) image of carotid 1; HR image obtained for $p = 1.5$ with (b)-the proposed method, (c)-the stationary PSF 1 and (d)-the stationary PSF 2; (e)-LR image of carotid 2; High resolution (HR) image obtained for $p = 1.3$ with (f)-the proposed method, (g)-the stationary PSF 1 and (h)-the stationary PSF 2.

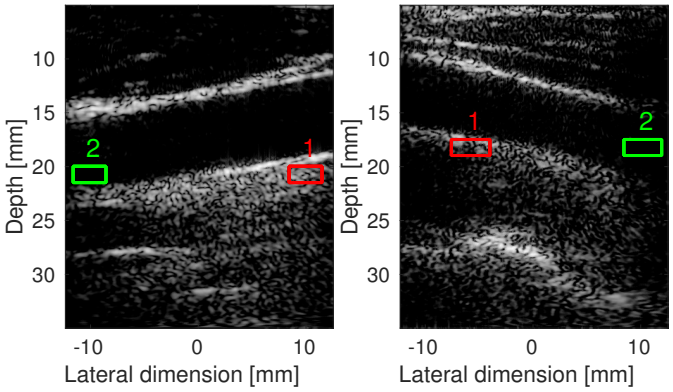

Fig. 8. Tissue (1) and blood (2) regions used for the computation of the tissue-to-clutter ratio and contras-to-noise ratio.

More precisely, we consider a PW experiment with the L11-4v probe described in Table I. We compare various grid sizes characterized by the corresponding values of N_x and N_z. For each tuple (N_x, N_z), we estimate the average evaluation time of the forward blur operator over 10 runs on an Intel Core i7-4930K CPU @ 3.40 GHz equipped with MATLAB R 2017A. We compare the proposed evaluation strategy, the one described by Roquette *et al.* [28] and the evaluation of a stationary blur model using Fourier domain approach.

Table VI reports the computation times of the three methods for the different grid sizes.

We can see that the proposed strategy is two orders of magnitude faster than the one developed by Roquette *et al.* even in the configuration with the smallest grid size. In addition, we observe significant differences in scaling between the two methods resulting from the difference in computational complexity.

We notice that the proposed strategy is several orders of magnitude slower than the stationary method. This is due to the fact that the Fourier-domain approach relies on fast Fourier transforms which have been highly optimized in MATLAB (built-in function) while the proposed approach entirely relies on a non-optimized MATLAB code. First implementations of the propagation and DAS operators on graphical processing units highlight the high potential for parallelizability of the proposed method [34], [33].

TABLE VI
COMPUTATION TIMES OF DIFFERENT BLUR EVALUATION STRATEGIES

(N_x, N_z)	Evaluation times		
	Roquette *et al.*	Proposed	Stationary
(64, 100)	3.5×10^{1} s	8.8×10^{-2} s	3.7×10^{-4} s
(128, 200)	3.4×10^{2} s	1.1×10^{-1} s	6.5×10^{-4} s
(256, 200)	1.6×10^{3} s	1.9×10^{-1} s	1.2×10^{-3} s

In addition, Figure 9 displays ratios of evaluation times between the proposed method and the stationary model for realistic values of the grid sizes. Indeed, we fix $N_x = 512$ which corresponds to one fourth wavelength spacing and we vary N_z between 1000 and 8000.

We empirically observe that the proposed methods scales better with the grid than the Fourier domain approach which corroborates the theoretical study of the complexity of Section III-E.

VI. CONCLUSION

This work presents a physically-based model of the non-stationary blur in the context of 2D ultrasound imaging. The model is based on the sequential application of a propagation

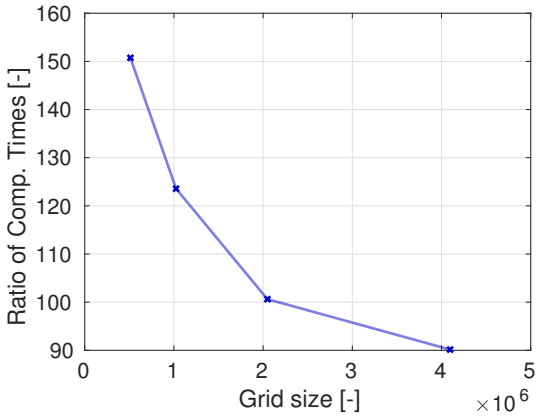

Fig. 9. Ratio of computational times between the proposed evaluation strategy and the Fourier domain evaluation of the stationary blur for varying grid sizes.

operator which relates the tissue-reflectivity function to the measured echo signals, and a delay-and-sum operator which forms the radio-frequency image from the echo signals.

Using this structure, we propose an evaluation strategy which exploits computationally efficient formulations of the involved operators, based on parametric formulations of time-of-flight equations, interpolation on appropriate grids and discrete convolutions. We demonstrate theoretically that such formulations allow the blur operator to scale linearly with the number of grid points and we show the benefits of this in practical scenarios.

In addition, the proposed model is presented in the context of common approximations of non-stationary blur operators. We show that while it seems to be similar to sectional methods, it is by essence different since sub-regions are selected by physical effects due to ultrasound propagation rather than arbitrarily as in sectional methods. We nevertheless state that the proposed model can be used in the context of sectional methods as well as for shift-invariant modelling of the blur.

As an example application, we use the model for ultrasound image restoration using maximum-a-posteriori estimation. We demonstrate through simulated and *in vivo* examples that the restoration approach with the proposed model can outperform most recent state-of-the-art restoration methods based on a stationary model of the blur.

Appendix A
Fast Iterative Shrinkage Thresholding Algorithm and Proximity Operators

A. Fast Iterative Shrinkage Thresholding Algorithm

This section briefly presents the fast iterative shrinkage thresholding algorithm (FISTA) used to solve Problem (51). For an in-depth description of the method, please refer to [47]. FISTA is an accelerated version of the well-known iterative soft thresholding algorithm (ISTA), that can be used to solve the following problem:

$$\min_{\boldsymbol{x}\in\mathbb{R}^N} \|\boldsymbol{y}-\boldsymbol{A}\boldsymbol{x}\|_2^2 + \phi(\boldsymbol{x}), \tag{55}$$

where $\boldsymbol{y}\in\mathbb{R}^M$, $\boldsymbol{x}\in\mathbb{R}^N$, $\boldsymbol{A}\in\mathbb{R}^{M\times N}$, $\phi:\mathbb{R}^N\to\mathbb{R}$ is a non-smooth convex regularizer.

In order to solve Problem (55), FISTA is composed of an acceleration step and a proximal gradient steps described in Algorithm 1. The proximal gradient step involves the following proximity operator [50]:

$$\text{prox}_\phi(\boldsymbol{x};\lambda) = \arg\min_{\boldsymbol{z}\in\mathbb{R}^N} \lambda\phi(\boldsymbol{z}) + \frac{1}{2}\|\boldsymbol{z}-\boldsymbol{x}\|_2^2. \tag{56}$$

Algorithm 1 FISTA used to solve Problem (55)

Require: $\boldsymbol{A}, \phi, \boldsymbol{y}, L \geq \lambda_{max}\left(\boldsymbol{A}^T\boldsymbol{A}\right)$
  initialization: $i=1, t_0=1, \boldsymbol{x}_{-1}=\boldsymbol{x}_0=\boldsymbol{0}$
  repeat
    $t_i \leftarrow \frac{1+\sqrt{1+4t_{i-1}^2}}{2}, \quad \alpha_i \leftarrow \frac{1-t_{i-1}}{t_i}$
    $\boldsymbol{c}_i \leftarrow \alpha_i\boldsymbol{x}_{i-2} + (1-\alpha_i)\boldsymbol{x}_{i-1}$
    $\boldsymbol{x}_i \leftarrow \text{prox}_\phi\left(\boldsymbol{c}_i + \frac{1}{L}\boldsymbol{A}^T(\boldsymbol{y}-\boldsymbol{A}\boldsymbol{c}_i); \frac{1}{L}\right)$
    $i \leftarrow i+1$
  until stopping criterion
  return $\boldsymbol{x}_i$

In Algorithm 1, $\lambda_{max}\left(\boldsymbol{A}^T\boldsymbol{A}\right)$ denotes the highest eigenvalue of $\boldsymbol{A}^T\boldsymbol{A}$.

B. Proximity operators associated with the ℓ_p-norm

We consider the proximity operator defined in (56), where $\phi(\boldsymbol{x}) = \|\boldsymbol{x}\|_p^p$ and $p\geq 1$. Thanks to the separability of the two functions involved in the proximity operator, the problem can be solved element-wise. According to Table 10.2 of [50], the following equivalence holds:

$$z_i = \arg\min_{z_i\in\mathbb{R}} \lambda|z_i|^p + \frac{1}{2}(z_i-x_i)^2, \ \forall(x_i,z_i)\in\mathbb{R}\times\mathbb{R}, \ \lambda>0 \tag{57}$$

$$\Leftrightarrow z_i = \text{sign}(x_i)\,q, \ q\geq 0, \ q+p\lambda q^{p-1} = |x_i|. \tag{58}$$

Thus, in order to derive the proximity operator associated with the ℓ_p-norm, one has to solve (58), which, in the general case, involves finding roots of a polynomial with arbitrarily high degree and can be achieved using Newton's method.

For specific values of p, the polynomial may have a degree lower or equal to 3. In such cases, (58) has an analytical solution. This is the case for the values of p considered in the study:

a) Case $p=1$: The solution of (58) is immediately deduced as:

$$z_i = \text{sign}(x_i)\max(|x_i|-\lambda, 0), \tag{59}$$

which is the well-known soft-thresholding operator.

b) Case $p=3/2$: The solution of (58) involves to find the positive root of the following polynomial of order 2:

$$0 = q + \frac{3}{2}\lambda q^{1/2} - |x_i| \tag{60}$$

$$\Leftrightarrow 0 = q^2 - \left(2|x_i| - \frac{9}{4}\lambda^2\right)q + x_i^2, \ |x_i|\geq q \tag{61}$$

$$\Leftrightarrow q = |x_i| + \frac{9}{8}\lambda\left(\lambda - \sqrt{\frac{16}{9}|x_i|+\lambda^2}\right). \tag{62}$$

c) Case $p = 4/3$: The solution of (58) involves to find the positive root of the following polynomial of order 3:

$$0 = q + \frac{4}{3}\lambda q^{1/3} - |x_i| \tag{63}$$

$$\Leftrightarrow 0 = q^3 - 3|x_i|q^2 + \left(3|x_i|^2 + \frac{64}{27}\lambda^3\right) q - |x_i|^3. \tag{64}$$

Using Cardano's method and after several calculations not detailed here, one may obtain the following value of q:

$$q = |x_i| + \frac{1}{9}\left(\frac{16 \cdot 2^{1/3} \cdot \lambda^2}{(z + 27|x_i|)^{1/3}} - 2\lambda\,(z + 27|x_i|)^{1/3}\right) \tag{65}$$

$$z = \sqrt{256\lambda^3 + 729|x_i|^2}. \tag{66}$$

References

[1] F. Sroubek, J. Kamenicky, and Y. M. Lu, "Decomposition of Space-Variant Blur in Image Deconvolution," *IEEE Signal Process. Lett.*, vol. 23, no. 3, pp. 346–350, mar 2016.

[2] L. Denis, E. Thiébaut, F. Soulez, J. M. Becker, and R. Mourya, "Fast Approximations of Shift-Variant Blur," *Int. J. Comput. Vis.*, vol. 115, no. 3, pp. 253–278, apr 2015.

[3] M. Hirsch, S. Sra, B. Schölkopf, and S. Harmeling, "Efficient filter flow for space-variant multiframe blind deconvolution," in *Proc. IEEE Comput. Soc. Conf. Comput. Vis. Pattern Recognit.*, aug 2010, pp. 607–614.

[4] J. G. Nagy and D. P. O'Leary, "Restoring Images Degraded by Spatially Variant Blur," *SIAM J. Sci. Comput.*, vol. 19, no. 4, pp. 1063–1082, jul 1998.

[5] C. Preza and J.-A. Conchello, "Depth-variant maximum-likelihood restoration for three-dimensional fluorescence microscopy," *J. Opt. Soc. Am. A*, vol. 21, no. 9, p. 1593, sep 2004.

[6] J. Bardsley, S. Jefferies, J. Nagy, and R. Plemmons, "A computational method for the restoration of images with an unknown, spatially-varying blur." *Opt. Express*, vol. 14, no. 5, pp. 1767–1782, mar 2006.

[7] M. I. Florea, A. Basarab, D. Kouame, and S. A. Vorobyov, "An Axially Variant Kernel Imaging Model Applied to Ultrasound Image Reconstruction," *IEEE Signal Process. Lett.*, vol. 25, no. 7, pp. 961–965, jul 2018.

[8] D. Miraut and J. Portilla, "Efficient shift-variant image restoration using deformable filtering (Part I)," *EURASIP J. Adv. Signal Process.*, vol. 2012, no. 1, pp. 1–20, may 2012.

[9] R. C. Flicker and F. J. Rigaut, "Anisoplanatic deconvolution of adaptive optics images." *J. Opt. Soc. Am.*, vol. 22, no. 3, pp. 504–513, mar 2005.

[10] T. Hrycak, S. Das, G. Matz, and H. G. Feichtinger, "Practical estimation of rapidly varying channels for OFDM systems," *IEEE Trans. Commun.*, vol. 59, no. 11, pp. 3040–3048, sep 2011.

[11] P. Escande and P. Weiss, "Sparse Wavelet Representations of Spatially Varying Blurring Operators," *SIAM J. Imaging Sci.*, vol. 8, no. 4, pp. 2976–3014, dec 2015.

[12] J. Wei, C. A. Bouman, and J. P. Allebach, "Fast space-varying convolution using matrix source coding with applications to camera stray light reduction," *IEEE Trans. Image Process.*, vol. 23, no. 5, pp. 1965–1979, may 2014.

[13] W. Vollmann, "Resolution enhancement of ultrasonic B-scan images by deconvolution," *IEEE Trans. Sonics Ultrason.*, vol. 29, no. 2, pp. 78–82, mar 1982.

[14] C. N. Liu, M. Fatemi, and R. C. Waag, "Digital processing for improvement of ultrasonic abdominal images," *IEEE Trans. Med. Imaging*, vol. 2, no. 2, pp. 66–75, jun 1983.

[15] T. Loupas, S. D. Pye, and W. N. McDicken, "Deconvolution in medical ultrasonics: practical considerations," *Phys. Med. Biol.*, vol. 34, no. 11, pp. 1691–1700, nov 1989.

[16] Z. Chen, A. Basarab, and D. Kouame, "Compressive deconvolution in medical ultrasound imaging," *IEEE Trans. Med. Imaging*, vol. 35, no. 3, pp. 728–737, mar 2016.

[17] U. R. Abeyratne, A. P. Petropulu, and J. M. Reid, "Higher order spectra based deconvolution of ultrasound images," *IEEE Trans. Ultrason. Ferroelectr. Freq. Control*, vol. 42, no. 6, pp. 1064–1075, nov 1995.

[18] T. Taxt, "Comparison of cepstrum-based methods for radial blind deconvolution of ultrasound images," *IEEE Trans. Ultrason. Ferroelectr. Freq. Control*, vol. 44, no. 3, pp. 666–674, may 1997.

[19] T. Taxt and J. Strand, "Two-dimensional noise-robust blind deconvolution of ultrasound images," *IEEE Trans. Ultrason. Ferroelectr. Freq. Control*, vol. 48, no. 4, pp. 861–867, jul 2001.

[20] J. Jensen, "Estimation of in vivo pulses in medical ultrasound," *Ultrason. Imaging*, vol. 16, no. 3, pp. 190–203, jul 1994.

[21] T. Taxt, "Radial homomorphic deconvolution of B-mode medical ultrasound images," in *Proc. 12th IAPR Int. Conf. Pattern Recognit.*, aug 1994, pp. 149–152.

[22] G. Demoment, R. Reynaud, and A. Herment, "Range resolution improvement by a fast deconvolution method," *Ultrason. Imaging*, vol. 6, no. 4, pp. 435–451, oct 1984.

[23] J. Jensen and S. Leeman, "Nonparametric estimation of ultrasound pulses," *IEEE Trans. Biomed. Eng.*, vol. 41, no. 10, pp. 929–936, oct 1994.

[24] O. Michailovich and A. Tannenbaum, "Blind deconvolution of medical ultrasound images: A parametric inverse filtering approach," *IEEE Trans. Image Process.*, vol. 16, no. 12, pp. 3005–3019, dec 2007.

[25] R. Demirli and J. Saniie, "Model-based estimation of ultrasonic echoes part I: Analysis and algorithms," *IEEE Trans. Ultrason. Ferroelectr. Freq. Control*, vol. 48, no. 3, pp. 787–802, may 2001.

[26] D. Iraca, L. Landini, and L. Verrazzani, "Power spectrum equalization for ultrasonic image restoration," *IEEE Trans. Ultrason. Ferroelectr. Freq. Control*, vol. 36, no. 2, pp. 216–222, mar 1989.

[27] O. V. Michailovich, "Non-stationary blind deconvolution of medical ultrasound scans," in *Prog. Biomed. Opt. Imaging - Proc. SPIE*, vol. 10139, mar 2017, p. 101391C.

[28] L. Roquette, M. Simeoni, P. Hurley, and A. Besson, "On an analytical, spatially-varying, point-spread-function," in *2017 IEEE Int. Ultrason. Symp.*, sep 2017.

[29] O. Michailovich and D. Adam, "A novel approach to the 2-D blind deconvolution problem in medical ultrasound," *IEEE Trans. Med. Imaging*, vol. 24, no. 1, pp. 86–104, jan 2005.

[30] H. Gomersall, D. Hodgson, R. Prager, N. Kingsbury, G. Treece, and A. Gee, "Efficient implementation of spatially-varying 3-D ultrasound deconvolution," *IEEE Trans. Ultrason. Ferroelectr. Freq. Control*, vol. 58, no. 1, pp. 234–238, jan 2011.

[31] G. David, J.-L. Robert, B. Zhang, and A. F. Laine, "Time domain compressive beam forming of ultrasound signals," *J. Acoust. Soc. Am.*, vol. 137, no. 5, pp. 2773–2784, may 2015.

[32] G. S. Alberti, H. Ammari, F. Romero, and T. Wintz, "Mathematical analysis of ultrafast ultrasound imaging," *SIAM J. Appl. Math.*, vol. 77, no. 1, pp. 1–25, jan 2017.

[33] A. Besson, D. Perdios, F. Martinez, Z. Chen, R. E. Carrillo, M. Arditi, Y. Wiaux, and J.-P. Thiran, "Ultrafast ultrasound imaging as an inverse problem: Matrix-free sparse image reconstruction," *IEEE Trans. Ultrason. Ferroelectr. Freq. Control*, pp. 1–1, 2017.

[34] A. Besson, D. Perdios, F. Martinez, M. Arditi, Y. Wiaux, and J.-P. Thiran, "USSR: An ultrasound sparse regularization framework," in *2017 IEEE Int. Ultrason. Symp.*, sep 2017.

[35] M. Alessandrini, S. Maggio, J. Poree, L. De Marchi, N. Speciale, E. Franceschini, O. Bernard, and O. Basset, "A restoration framework for ultrasonic tissue characterization," *IEEE Trans. Ultrason. Ferroelectr. Freq. Control*, vol. 58, no. 11, pp. 2344–2360, nov 2011.

[36] M. Vetterli, J. Kovačević, and V. K. Goyal, *Foundations of Signal Processing*. Cambridge University Press, sep 2014.

[37] M. F. Schiffner and G. Schmitz, "Fast pulse-echo ultrasound imaging employing compressive sensing," in *2011 IEEE Int. Ultrason. Symp.*, oct 2011.

[38] P. R. Stepanishen, "The time-dependent force and radiation impedance on a piston in a rigid infinite planar baffle," *J. Acoust. Soc. Am.*, vol. 49, no. 1A, pp. 76–76, jan 1971.

[39] A. R. Selfridge, G. S. Kino, and B. T. Khuri-Yakub, "A theory for the radiation pattern of a narrow-strip acoustic transducer," *Appl. Phys. Lett.*, vol. 37, no. 1, p. 35, apr 1980.

[40] J. Jensen and N. Svendsen, "Calculation of pressure fields from arbitrarily shaped, apodized, and excited ultrasound transducers," *IEEE Trans. Ultrason. Ferroelectr. Freq. Control*, vol. 39, no. 2, pp. 262–267, mar 1992.

[41] G. Montaldo, M. Tanter, J. Bercoff, N. Benech, and M. Fink, "Coherent plane-wave compounding for very high frame rate ultrasonography and transient elastography," *IEEE Trans. Ultrason. Ferroelectr. Freq. Control*, vol. 56, no. 3, pp. 489–506, mar 2009.

[42] C. Papadacci, M. Pernot, M. Couade, M. Fink, and M. Tanter, "High-contrast ultrafast imaging of the heart," *IEEE Trans. Ultrason. Ferroelectr. Freq. Control*, vol. 61, no. 2, pp. 288–301, feb 2014.

[43] V. Dumoulin and F. Visin, "A guide to convolution arithmetic for deep learning," vol. 587, mar 2016.

[44] N. Zhao, Q. Wei, A. Basarab, D. Kouame, and J.-Y. Tourneret, "Blind deconvolution of medical ultrasound images using a parametric model for the point spread function," in *2016 IEEE Int. Ultrason. Symp.*, sep 2016.
[45] R. Morin, S. Bidon, A. Basarab, and D. Kouame, "Semi-blind deconvolution for resolution enhancement in ultrasound imaging," in *2013 IEEE Int. Conf. Image Process.*, sep 2013, pp. 1413–1417.
[46] O. Scherzer, H. Grossauer, F. Lenzen, M. Grasmair, and M. Haltmeier, *Variational Methods in Imaging*, ser. Applied Mathematical Sciences. New York, NY: Springer New York, 2009, vol. 167.
[47] A. Beck and M. Teboulle, "A fast iterative shrinkage-thresholding algorithm for linear inverse problems," *SIAM J. Imaging Sci.*, vol. 2, no. 1, pp. 183–202, jan 2009.
[48] M. C. Van Wijk and J. M. Thijssen, "Performance testing of medical ultrasound equipment: Fundamental vs. harmonic mode," *Ultrasonics*, vol. 40, no. 1-8, pp. 585–591, may 2002.
[49] ——, "Performance testing of medical ultrasound equipment: Fundamental vs. harmonic mode," *Ultrasonics*, vol. 40, pp. 585–591, 2002.
[50] P. L. Combettes and J.-C. Pesquet, "Proximal Splitting Methods in Signal Processing," in *Fixed-Point Algorithms Inverse Probl. Sci. Eng.* Springer New York, 2011, vol. 49, pp. 185–212.